Mechanisms for thermal conduction in various polymorphs of methane hydrate

Niall J. English,[1,*,†] John S. Tse,[2,*,‡] and Declan J. Carey[1,§]

[1]*The SEC Strategic Research Cluster and the Centre for Synthesis and Chemical Biology, School of Chemical and Bioprocess Engineering, Conway Institute of Biomolecular and Biomedical Research, University College Dublin, Belfield, Dublin 4, Ireland*

[2]*Department of Physics and Engineering Physics, University of Saskatchewan, Saskatoon, Saskatchewan, Canada S7N 5E2*

Extensive equilibrium molecular-dynamics simulations have been performed to investigate thermal-conduction mechanisms via the Green-Kubo approach for fully occupied type I, II, and H methane hydrates, in addition to ice Ih and a hypothetical empty type I hydrate structure. The TIP4P water model was used in conjunction with a fully atomistic methane potential with which it had been parameterized from quantum simulation, along with long-range Ewald electrostatics. We have found that the crystal structure of the clathrate framework and guest-host interactions in type I methane hydrate contribute to a lower thermal conductivity vis-à-vis ice Ih and its glasslike temperature dependence, respectively; damping in methane-host energy transfer above 100 K was determined to be responsible for the latter. However, we have found that substantially less damping in guest-host energy transfer is present in type II and H methane-hydrate polymorphs at higher temperatures, giving rise to somewhat larger thermal conductivities relative to type I methane hydrate with a crystal-like temperature dependence.

I. INTRODUCTION

Clathrate hydrates are nonstoichiometric crystalline inclusion compounds in which a water host lattice encages small guest atoms or molecules in cavities; the empty lattice is thermodynamically unstable, and its existence is due to hydrogen-bond stabilization resulting from the enclathration of the trapped solutes in its cages.[1,2] There are three known common hydrate structures: (s)I, II, and H. In type I hydrate, the unit cell is formed from two small 5^{12} pentagonal dodecahedral cavities and six slightly larger tetrakaidecahedral $5^{12}6^2$ cages, with 46 water molecules.[1,2] In sII clathrate, each unit cell contains 136 water molecules and 24 cages, 16 of which are small 5^{12} cavities and eight of which are medium-sized 16-hedra $5^{12}6^4$ while sH unit cells are composed of 34 water molecules with three small 5^{12} cages, two small 12-hedra $4^35^66^3$ cavities and one large 18-hedra $5^{12}6^8$ cage.[1,2] The average effective radii of cages are approximately 3.7 Å for 5^{12}, 4.0 Å for $5^{12}6^2$, 4.2 Å for $5^{12}6^4$, 4.1 Å for $4^35^66^3$, and 5.7 Å for $5^{12}6^8$.[1,2] For type I methane hydrate, there are up to eight guests per unit cell (i.e., one per cavity), with up to 24 methane molecules for sII (i.e., one per cavity) and up to ten methanes per unit cell in sH (one per each small cage and up to five in the large cage[3]). Methane hydrates are the most widespread type of clathrate and are thought to exist in nature primarily as type I in the permafrost and deep ocean regions with methane compositions of around 90% of the maximum theoretical occupation, and constitute a possible significant energy resource.[4,5] However, at higher pressures, sII and sH structures of methane hydrate become stable at temperatures of practical interest, and it is thought that some segments of natural methane-hydrate deposits may adopt the sII polymorph in pressurized environments.[6] The most peculiar property of (type I) methane hydrate is its very low thermal conductivity compared to ice. Moreover, above around 100 K, its conductivity displays a weak temperature dependence, resembling amorphous solids.[7,8] It is clear that a detailed understanding of thermal-conduction mechanisms in the various polymorphs of methane hydrate would be beneficial in terms of large-scale exploitation of hydrate deposits as an energy source.

In addition to clathrate hydrates, anomalous "glasslike" thermal-conductivity behavior is shared by some clathratelike compounds, e.g., metal-Si clathrates[9] and skutterudites.[10] Currently, there is no theory to explain this unusual thermal-transport phenomenon. Several hypotheses have been suggested to explain this observation, the most studied being the "resonant scattering" model,[8,11–14] which originates in hydrates from "avoided crossings" of lattice acoustic phonons with localized guest vibrations of identical symmetry[11–13] dissipating heat transport. Experimental measurements of thermal conductivity in (type I) methane hydrate exhibit a crystal-like temperature dependence below 90 K, with glasslike behavior above this temperature.[15] Similar low-temperature behavior is observed in some semiconductor clathrates.[16] The objective of the current study is to predict thermal conductivities in type I methane hydrates and the higher-pressure sII and sH polymorphs over a wide temperature range using equilibrium molecular dynamics (MD),[17] and to investigate in detail the influence and importance of (guest-host) energy-transfer processes thereon. The outline of the paper is as follows: (i) the computational methods shall be described with a strong emphasis on technical aspects; (ii) the procedures for extracting relevant physical quantities, such as various time-correlation functions, thermal conductivity, relaxation times, *interalia* are discussed; (iii) the role of the water framework and methane molecules in the transport of thermal energy is analyzed; (iv) a discussion on the mechanisms responsible for thermal conduction in different hydrate polymorphs is provided to end the paper.

II. METHODOLOGY

The TIP4P water model was used for water-water interactions[18] and the all-atom Optimized Potentials for Liq-

uid Simulations (OPLS-AA) potential for methane-methane interactions.[19] The bond lengths and angles in methane were constrained to their experimental values, i.e., a C-H length of 1.09 Å and an H-C-H angle of 109.47°. To obtain the best accuracy possible for methane-hydrate simulation, in which water and methane molecules are in close contact, the water-methane interaction parameters of Sun and Duan were used.[20] Briefly, the authors found that an accurate fit to their *ab initio* water-methane energy surface could be obtained if the experimental methane geometry was used along with the geometry and partial charges of TIP4P water. The partial charges which were fit to the methane sites were $-0.48e$ (C) and $0.12e$ (H), and appropriate Lennard-Jones interaction parameters were also fit to the *ab initio* data.[20] Mastny and de Pablo[21] have validated the use of TIP4P, rigid OPLS-AA methane and the Sun-Duan interaction parameters by a prediction of the melting point of (sI) methane hydrate at 400 bar to be within 287 and 302 K, via-à-vis the experimental value of 297 K. Although English and MacElroy[22] and Jiang *et al.*[23] have demonstrated previously that polarizable water models tend to be quantitatively superior for the treatment of methane hydrates, there have been few attempts made to date in hydrate simulation to use water and methane models and interaction parameters which have been parameterized specifically for water-methane systems.

The cutoff radius for Lennard-Jones interaction parameters was 12 Å. Following detailed validation with respect to the definitive Lekner method for thermal-conductivity estimation in (type I) methane hydrate,[24] the Ewald method was used to handle long-range electrostatic interactions.[25,26] The real-space cutoff distance for the Ewald method was 15 Å and the screening parameter and the number of wave vectors were set such that the relative error in the Ewald summation was less than 1×10^{-6}. In practice, this led to the product of the screening parameter α and the real-space cutoff distance to be in the range of around 3.2–3.5, and the Ewald electrostatic energy and forces varied very little with α and increasing number of wave vectors. The velocity Verlet scheme was used for MD,[26] and the RATTLE method used to impose constraints.[27] For extended system dynamics in the NVT ensemble, light coupling to a Nosé-Hoover thermostat was used, with a thermostat relaxation time of 1 ps.[28] Where dynamics was carried out in the NPT case, light coupling was applied with Melchionna's modified form of the Hoover barostat using isotropic cell fluctuations,[29] with thermostat and barostat relaxation times of 1 and 2.5 ps, respectively.

The starting coordinates of the oxygen atoms in the unit cells of sI, sII, and sH hydrates were taken from respective x-ray diffraction data.[30–32] The orthorhombic $5 \times 3 \times 3$-unit-cell proton-disordered configuration was treated as the fundamental cell for ice Ih.[33] The initial unit-cell lengths were 12.03 and 17 Å for the cubic sI and sII systems, respectively, and the parameters for the hexagonal sH cell were $a=12.212$ and $c=10.143$ Å. The initial orientations of the water molecules were selected in a random manner so as to conform to the Bernal-Fowler rules[34] and so that the total dipole moment of the system would be vanishingly small. For sI and sII, the Rahman-Stillinger procedure was used to achieve a small total dipole moment[35] while the dipole-minimized water orientation of Okano and Yasuoka was

taken for sH.[36] Methane molecules were placed in the cavities of each unit cell to allow for full occupation, i.e., eight methane molecules in sI, 24 in sII, and ten in sH; this corresponds to single occupancy of all cages, except five molecules in the large sH $5^{12}6^8$ cage, following Alavi *et al.*[3] This was done as previous MD simulation work has shown that (sI) methane-hydrate thermal conductivity is only weakly dependent on cage occupancy in the 80–100 % range (as a proportion of the maximum possible occupation).[37] The sH hexagonal unit cell was converted to a rectangular, orthorhombic geometry, with side lengths of 12.212, 10.576, and 10.143 Å. Simulation boxes were constructed by replication. For all simulations, $3 \times 3 \times 3$ sI, $2 \times 2 \times 2$ sII, and $3 \times 4 \times 4$ sH unit cells and $2 \times 2 \times 2$ fundamental ice cells were employed. An empty $3 \times 3 \times 3$ sI simulation box, bereft of methane molecules, was also prepared. Additional, larger occupied hydrate systems were simulated for validation of thermal-conductivity prediction at 265 K for the system sizes above, and consisted of $4 \times 4 \times 4$ sI, $4 \times 4 \times 4$ sII, and $4 \times 5 \times 5$ sH unit cells but it was found that use of these larger systems was not required for reliable estimates of thermal conductivity (cf. "Results"). Earlier validation of the adequate size of the $3 \times 3 \times 3$ sI methane hydrate was carried out for the Ewald technique with respect to both system size and the rigorous Lekner method for the potentials used.[24]

A 1 fs time step was used for all simulations. This time step was tested for energy conservation in the NVE ensemble and found to be satisfactory; the percentage relative drift in energy, defined as the ratio of the energy drift (expressed as a linear regression coefficient) to the average kinetic energy during the simulation,[38] was less than 0.1% over 100 ps in all cases. Between 0.5 and 3 ns of MD was carried out in the NPT ensemble for each starting structure of ice and hydrates (both occupied and empty), with set temperatures of 30, 100, 150, 200, and 220 K (ice)/265 K (sI hydrate) and a set pressure of 1 bar, respectively; TIP4P ice was found to melt above approximately 230 K, in accord with previous estimates for its melting point.[39] NPT relaxation was carried out at 20 and 30 kbar for sII and sH hydrates, respectively, as these hydrates becomes stable at these pressures.[6] Melchionna's modified form of the Hoover barostat with isotropic cell fluctuation was employed,[29] with light coupling from thermostat and barostat relaxation times of 1 and 2.5 ps, respectively. Once the system volumes had reached steady values with mean pressures at their set values, up to 2 ns of relaxation was performed in the NVT ensemble with light coupling to a Nosé-Hoover thermostat[28] with relaxation time of 1 ps. Shorter relaxation simulations (0.5 ns each of NPT and NVT) were carried out for sII $4 \times 4 \times 4$ and sH $4 \times 5 \times 5$ at 265 K, owing to their larger size. Subsequent NVE simulations were of 2–5 ns in duration, and the temperature and pressure remained within 1% and 2% of their desired values, respectively; although the empty hydrate is thermodynamically unstable relative to ice Ih, the ice and occupied/empty hydrate structures were observed to be stable throughout the relaxation and production stages.

The heat-flux vector **J** was evaluated by the microscopic expression in the molecular representation,[40,41]

$$VJ = \sum_{i=1}^{N} \mathbf{v}_i^{\text{c.m.}} e_i + \frac{1}{2} \sum_{i=1}^{N} \sum_{a=1}^{n_i} \sum_{j=1}^{N} \sum_{b=1}^{n_j} \mathbf{r}_{ij}^{\text{c.m.}} \mathbf{f}_{ia,jb} \cdot \mathbf{v}_{jb} - \sum_{\nu=1}^{2} h_\nu \sum_{i}^{N_\nu} \mathbf{v}_{i_\nu},$$

$$(1)$$

where N is the total number of molecules and ν denotes the species (water or methane). In the diffusive term, e_i refers to the internal energy of molecule i (i.e., the sum of its kinetic energy and its interaction energy with the rest of the system). In the interactive term, there is a pairwise summation over the forces exerted by atomic sites on one another. The species enthalpy correction term requires that the total enthalpy of the system is decomposed into contributions from each species (water and methane).[24,41] Due to the partial transformation from pairwise, real-space treatment to a reciprocal space form in Ewald electrostatics, it is necessary to recast the diffusive and interactive terms in this expression in a form amenable for use with the Ewald method. This was done in this work, using the recent reformulation of Petravic.[24,42] It has become known recently that truncations of long-range electrostatic interactions in charged systems lead to errors in the stress tensor,[43] and this shortcoming may affect the heat-flux vector and its autocorrelation function (ACF) markedly.[42] Therefore, the use of Ewald electrostatics with Petravic's reformulation was required for accurate treatment in this study, based on previous validation of electrostatics methods for sI methane hydrate.[24] The heat-flux vector was sampled every 1 fs in the production simulations.

The thermal conductivity was evaluated by the Green-Kubo (GK) time-correlation integral,[44] of the autocorrelation function of the heat-flux vector (JACF),

$$k = \frac{V}{3k_B T^2} \int_0^\infty \langle \mathbf{J}(t) \cdot \mathbf{J}(0) \rangle dt. \qquad (2)$$

The JACF was defined for 100 ps at 30 K, for 50 ps at 100 and 150 K, and for 20 ps at 200 K and above; a sampling ratio of approximately 30:1 or higher is recommended for a robust definition of the ACF.[37] These durations were found to be more than sufficient to provide a reliable estimate of the thermal conductivity at each temperature; the JACF had decayed essentially to zero within less than a quarter of the sampled time scales and oscillated about zero thereafter. Romberg integration was used to evaluate Eq. (2), with smooth cubic spline interpolation to generate the required artificial JACF values in between the sampling intervals.[45]

Relaxation times, related to energy-transfer times between neighboring atoms for phonon transport, may be extracted by fitting JACF's to sums of exponentially decaying functions, together with cosine-modulated terms for optic component decay.[46,47] The normalized JACF's were decomposed as follows:

$$\text{JACF}(t) = \sum_{i=1}^{n\_ac} A_i \exp(-t/\tau_i) + \sum_{j=1}^{n\_\text{opt}} \left[\sum_{k=1}^{n\_o,j} B_{jk} \exp(-t/\tau_{jk}) \right]$$

$$\times \cos \omega_{0,j} t + \sum_{j=1}^{n\_\text{opt}} C_j \cos \omega_{0,j} t, \qquad (3)$$

where there were either two or three phonon (as opposed to

"lattice") acoustic modes (short time, longer time, and, possibly, medium time), depending on hydrate occupation and temperature, and the optical modes were gauged with reference to peaks in the optical region of the power spectrum obtained from the Fourier transform (FT) of the JACF. The fitting procedure is described in detail in the Supplementary Information.[48] The constant amplitude term was applied to the optic modes to express the residual oscillation of the JACF about zero beyond the decay of the acoustic and optic modes, although it would be perhaps better to rationalize this as residual lattice acoustic modes (approximately 0.3–0.65 ps), modulated by optic-mode oscillation (cf. Fig. 3). However, this constant-term residual term is omitted in any analytic FT treatment, as it would result in a delta-function response in the power spectrum at that frequency (cf. Supplementary Information[48]). Here, $\omega_{0,j}$ are the optical peaks from the JACF's power spectrum (i.e., $500 - 1000$ cm^{-1} range). In practice, it was found that there was one main optical frequency mode (the main optic peak of the JACF's power spectrum) subject to relaxation, although there may have been more than one constant-term optic mode taken. The optic-modes' frequencies, $\omega_{0,j}$, may be determined by inspection of the JACF's power spectrum; the corresponding periods may be determined by finding the distribution of interval times between the successive peaks in the JACF, allowing one to rationalize this with respect to the peaks in the power spectrum.

III. RESULTS AND DISCUSSION

An advantage of using classical molecular-dynamics method in the study of thermal conductivity is that various contributions to the thermal-transport process can be delineated from the partition of the total into their separate components. Mechanisms for the exchange of (thermal) energy between atoms can be analyzed through calculations of appropriate time-correlation functions. The phonon-scattering processes may be characterized by distinct relaxation times. In the following sections, the convergence of the calculated thermal conductivities with respect to the choice of the system sizes will be validated. Then a comparison of the temperature-dependent thermal-conduction profiles of the hydrate polymorphs is made. In each case, the transport of thermal energy is investigated from an analysis of the total and partitioned (methane and water) heat-flux time-correlation functions. Relaxation-times characteristic of different processes will be extracted from the JACFs. Calculated self-energy and guest-host interaction energy time-correlation functions will be compared with appropriate vibrational spectra and correlated with characteristic relaxation times from the JACFs. Drawing from the conclusions of these analyses, atomistic mechanisms for thermal conduction in hydrate polymorphs are revealed.

A. Thermal conductivities

The results for the thermal conductivities of the hydrate systems at 265 K are presented below in Table I. These were found as the average of four independent runs with ACF's of

TABLE I. Comparison of the thermal conductivity of values obtained by simulation for the smaller and larger systems (in $Wm^{-1} K^{-1}$) at 265 K and 0.001, 20, and 30 kbar. Respectively, for sI, sII, and sH, the smaller systems are $3 \times 3 \times 3$, $2 \times 2 \times 2$, and $3 \times 4 \times 4$ while the larger systems are $4 \times 4 \times 4$, $4 \times 4 \times 4$, and $4 \times 5 \times 5$. The smaller systems were found to lead to satisfactory estimates and were used for thermal conductivity estimates at other temperatures.

	P (kbar)	Smaller	Larger
sI	0.001	0.64 ± 0.047	0.65 ± 0.048
sII	20	0.92 ± 0.063	0.94 ± 0.065
sH	30	0.95 ± 0.068	0.99 ± 0.070
Expt. (sI)	0.001	0.68^a, 0.62^b	0.68^a, 0.62^b

[a]Reference 37.
[b]Reference 49.

FIG. 1. Computed thermal conductivities for ice Ih, and sI, sII, sH, and empty sI methane hydrates from 30 to 265 K.

20 ps in duration, i.e., a sampling ratio of 100:1. The conductivities estimated from 20 ps ACF's (defined using sampling ratios of 100:1 over the full 2 ns duration) were in agreement with those in Table I (from 50 ps ACF's) to within a fraction of the standard deviation. Respectively, for sI, sII, and sH, the "smaller" systems are $3 \times 3 \times 3$, $2 \times 2 \times 2$, and $3 \times 4 \times 4$ while the "larger" systems are $4 \times 4 \times 4$, $4 \times 4 \times 4$, and $4 \times 5 \times 5$ unit cells. For the smaller systems, this corresponds to 1242 water and 216 methane molecules for sI, 1088 water and 192 methane molecules for sII, and 1,632 water and 480 methane molecules for sH while the corresponding respective values for the larger systems are 2944 and 512, 8704 and 1536, and 3400 and 100.

From Table I, it is seen that the sI result is in good agreement with reliable experimental values on compacted samples, and in accord with previous values using Ewald electrostatics and the current potentials.[24] For all structure types, there is only a small increase of about $3-4$ % in results for the larger systems relative to the "standard" ones used at all temperatures, which is within the estimate for the standard deviations. In previous work, it was shown that the average of the phonon mean-free-path distribution at 265 K ($3.7-3.9$ Å) is less than the unit-cell length for sI methane hydrate for the potentials used in this study.[24] Therefore, it is expected that the results for the larger systems do not exhibit any real further size effects vis-à-vis the standard systems.

The computed thermal conductivities are illustrated in Fig. 1 while experimental results for ice and sI hydrate are specified in Table II. Prior to discussing the conductivity results, however, it is worthwhile making some general remarks about crystalline thermal-conductivity behavior. A crystal's thermal-conductivity's temperature profile is well known. Above half of the Debye temperature, $\Theta_D/2$, the thermal conductivity exhibits a T^{-1} dependence, explained by Umklapp processes scattering phonons.[51,52] (For methane hydrate, Θ_D is 226 K.[53]) Thermal conductivity increases as temperature decreases below $\Theta_D/2$, reaching a maximum near $\Theta_D/10$. In this "intermediate" régime, the thermal-conductivity's absolute value is heavily dependent on defects. Below around $\Theta_D/10$, conductivity has T^3 dependence,
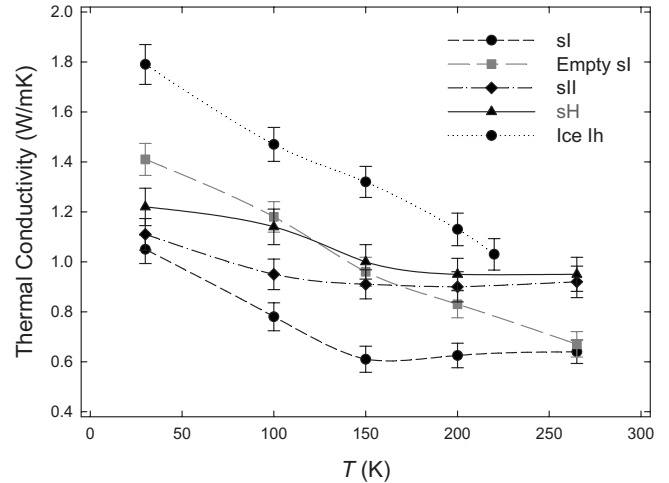
governed mainly by boundary scatterings. Therefore, experimental determination of thermal conductivity is highly dependent on samples' nature and quality, which has been outlined in some detail for methane hydrates.[15,37,49] This underlines the difficulty in a quantitative comparison of theoretical and experimental values, as previous joint experimental-simulation research for methane hydrate has shown.[37] It should also be noted that classical theory is expected to be valid at temperatures above one tenth of the Debye temperature ($\Theta_D/10$), i.e., approximately 20 K for (sI) methane hydrate.

The calculated conductivity for sI hydrate at 265K of 0.64 ± 0.05 $Wm^{-1} K^{-1}$ agrees with experiments on highly mechanically compacted samples with low porosity[37,49] giving $0.62-0.68$ $Wm^{-1} K^{-1}$ (cf. Table II). Although the calculated ice Ih conductivity at 220 K of 1.03 ± 0.05 $Wm^{-1} K^{-1}$, is lower than the experimental value[50] of 2.4 $Wm^{-1} K^{-1}$, it is consistent with a previous calculation by the TIP4P potential.[54] The lower absolute computed conductivity values for ice in quantitative comparison to experiment[50] is likely due to imperfections of the interaction potential models. Quantum effects are expected to be negligible at temperatures higher than 20 K.[55] In fact, it has been shown previously from neutron inelastic-scattering experiments[11] on methane hydrate that classical behavior is valid for temperature higher than 30 K. Significantly, the correct trends in crystalline behavior of ice is predicted, and similarly for empty sI and sH hydrates. The temperature profile of sI hydrate is quite different: from 265 to 150 K, conductivity is *lower* than the empty hydrate, decreasing slightly with temperature. A conductivity minimum is predicted at 100–150 K, then increasing thermal conductivity with decreasing temperature. The temperature behavior in this region parallels that of amorphous ice, with its "glassy" dependence.[56] The thermal-conductivity behavior of sII hydrate is somewhat intermediate between sI and fully crystalline ice, empty sI and sH hydrates, with a slight increase in thermal conductivity between 200 and 265 K. These observations are consistent with expectations. Both empty sI and sH hydrates are expected to be crystallinelike, as the empty sI structure has no

TABLE II. Acoustic relaxation times and contributions to the overall estimated thermal conductivity based on fitting procedure, along with experimental thermal conductivities (where available), in $Wm^{-1} K^{-1}$.

Type	T (K)	$\tau_{sh,ac}$ (ps)	Short-range acoustic	$\tau_{int,ac}$ (ps)	Medium-range acoustic	$\tau_{lg,ac}$ (ps)	Long-range acoustic	Optic	Total	Experiment
sI	30	0.38 ± 0.062	0.21			$4.4 \pm .39$	0.69	0.15	1.05 ± 0.057	0.48[a]
	100	0.22 ± 0.043	0.10			$3.6 \pm .26$	0.54	0.14	0.78 ± 0.056	0.42[a]
	150	0.063 ± 0.008	0.05	0.39 ± 0.21	0.04	$3.5 \pm .30$	0.40	0.12	0.61 ± 0.052	0.44[a]
	200	0.048 ± 0.006	0.06	0.37 ± 0.19	0.05	$2.9 \pm .24$	0.39	0.13	0.63 ± 0.049	0.45[a]
	265	0.046 ± 0.005	0.06	0.33 ± 0.16	0.05	$2.1 \pm .27$	0.40	0.13	0.64 ± 0.047	0.68[b],0.62[c]
Empty sI	30	0.44 ± 0.056	0.20			$6.1 \pm .49$	0.99	0.22	1.41 ± 0.064	
	100	0.24 ± 0.030	0.18			$4.5 \pm .38$	0.82	0.18	1.18 ± 0.061	
	150	0.112 ± 0.013	0.15			$4.1 \pm .45$	0.67	0.14	0.96 ± 0.058	
	200	0.072 ± 0.0061	0.17			$2.8 \pm .32$	0.50	0.16	0.83 ± 0.054	
	265	0.057 ± 0.0047	0.08			$2.2 \pm .23$	0.43	0.16	0.67 ± 0.051	
Ice	30	0.47 ± 0.068	0.24			$8.2 \pm .58$	1.31	0.24	1.79 ± 0.080	28[d]
	100	0.38 ± 0.061	0.17			$7.5 \pm .45$	1.09	0.21	1.47 ± 0.076	5.0[d]
	150	0.33 ± 0.054	0.16			$6.4 \pm .56$	0.93	0.23	1.32 ± 0.067	3.8[d]
	200	0.28 ± 0.031	0.13			$2.9 \pm .37$	0.79	0.21	1.13 ± 0.065	2.5[d]
	220	0.23 ± 0.034	0.11			$2.4 \pm .23$	0.72	0.20	1.03 ± 0.066	2.4[d]
sII	30	0.32 ± 0.021	0.18			$7.5 \pm .64$	0.68	0.25	1.11 ± 0.063	
	100	0.21 ± 0.019	0.14			$5.2 \pm .41$	0.61	0.20	0.95 ± 0.061	
	150	0.081 ± 0.0072	0.10			$4.2 \pm .38$	0.62	0.19	0.91 ± 0.058	
	200	0.064 ± 0.0047	0.10			$3.9 \pm .34$	0.62	0.18	0.90 ± 0.060	
	265	0.056 ± 0.0044	0.08	0.30 ± 0.14	0.11	$3.1 \pm .29$	0.57	0.16	0.92 ± 0.063	
sH	30	0.31 ± 0.040	0.17			$6.2 \pm .38$	0.81	0.24	1.22 ± 0.075	
	100	0.20 ± 0.028	0.15			$5.3 \pm .34$	0.77	0.22	1.14 ± 0.071	
	150	0.069 ± 0.0086	0.11			$3.4 \pm .27$	0.69	0.20	1.00 ± 0.069	
	200	0.055 ± 0.0071	0.10			$3.1 \pm .17$	0.68	0.17	0.95 ± 0.064	
	265	0.046 ± 0.0058	0.07	0.27 ± 0.14	0.12	$2.6 \pm .22$	0.62	0.14	0.95 ± 0.068	

[a]Reference 15.
[b]Reference 37.
[c]Reference 49 from low-porosity and well-compacted samples.
[d]Reference 50.

phonon scattering by guests, and there are no localized guest vibrations in sH due to the cavity structure, as evidenced experimentally by the absence of avoided crossing in x-ray inelastic-scattering experiments,[57] and shown in carbon-atoms' velocity ACF power spectra (*vide infra*). On the other hand, given that the resonance-scattering model provides a mechanism of dissipation of heat transport in the water lattice through energy absorption by guests of heat energy, a consequence of this model is that phonon scattering will be relatively inefficient if the temperature (thermal energy) is lower than the rattling vibrations. This conjecture is supported by recent experiments on (sI) methane (Ref. 15) and Xe (Ref. 58) hydrates extended to very low temperatures. In methane hydrate, glasslike thermal conductivity is no longer observed experimentally at temperatures below 90 K (i.e., 60 cm^{-1} energy[11,13]); thermal conductivity increases with decreasing temperature, reaching a maximum at 40 K, not unlike a crystal,[15] although recent nonequilibrium MD work could not confirm this trend conclusively.[59] Similar low-temperature behavior has also been reported in some semi-

conductor clathrates.[16] These findings show that the present theoretical results are reliable semiquantitatively.

B. Heat-flux ACF's and power spectra

An advantage of the Green-Kubo approach is that various modes contributing to the thermal conductivity may be gleaned from careful analysis of relevant components of the JACF. Normalized heat-flux ACF's (JACF's) are shown in Figs. 2 and 3 for ice, and sI, sII, sH, and empty sI hydrates, for short and long times at 200 and 30 K, respectively. JACF's are usually characterized by two relaxation times—a rapid initial drop followed by a long decay.[60] In the case of ice and hydrate polymorphs, the JACF decay is modulated by oscillatory features, which arise from localized optic modes, i.e., water librations, in addition to lattice and/or guest acoustic modes, or lattice-guest coupling modes (0.3–0.65 ps). The optic oscillations are typically 35–43 fs in duration (around 775–950 cm^{-1}), depending on the structure (e.g., ice, sI, etc.) and temperature, and are visible clearly in
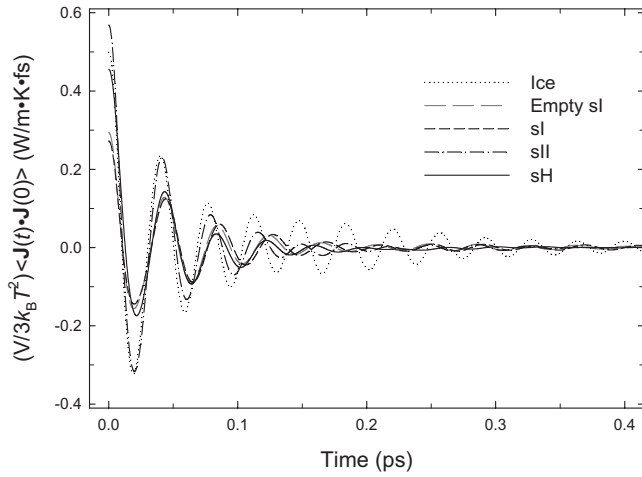
FIG. 2. Short-time normalized JACF's for ice Ih, and sI, sII, sH, and empty sI hydrates at 200 K.

Figs. 2 and 3; this will be linked to the librational lattice spectra discussed below. In Fig. 2, it is evident that ice has a larger amplitude of optic contribution in its short-time decay, leading to a larger optic thermal conductivity. In Fig. 3, the lattice acoustic-mode oscillations are evident in the modulation of the long-time constant-amplitude behavior after the decay of the acoustic phonon modes and short-time optical relaxation, with the optic-modes' periodicity superimposed thereon. This is especially apparent at lower temperature, with larger-amplitude "residual" acoustic lattice/guest modes. Estimates of the periods of lattice/guest acoustic modes at 30 K were also depicted in Fig. 3. For ice, these are approximately 0.42 and 0.64 ps (52 and 79 cm^{-1}); for sI, 0.4 and 0.52 ps (64 and 83 cm^{-1}); for empty sI, 0.45 and 0.65 ps (51 and 74 cm^{-1}); for sII, 0.30 and 0.44 ps (76 and 111 cm^{-1}); and for sH, 0.35 ps (98 cm^{-1}). These overlap quite well with the lattice/guest acoustic modes at 30 K, as evidenced by power spectra of the oxygen and carbon atoms' VACF's (see Sec. III E).

Power spectra of the normalized JACF's [the integral of which gives k in Eq. (2)] were evaluated by real-space Fou-
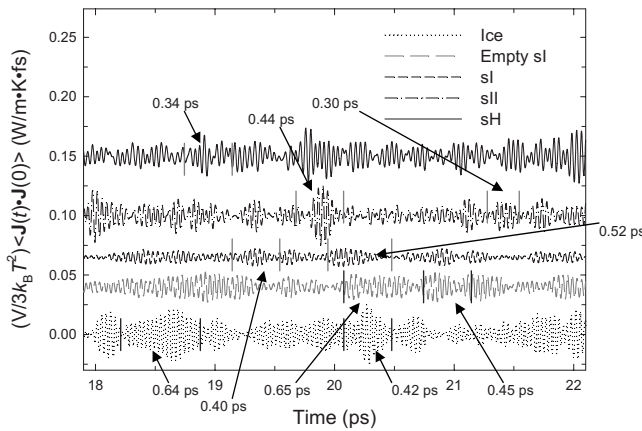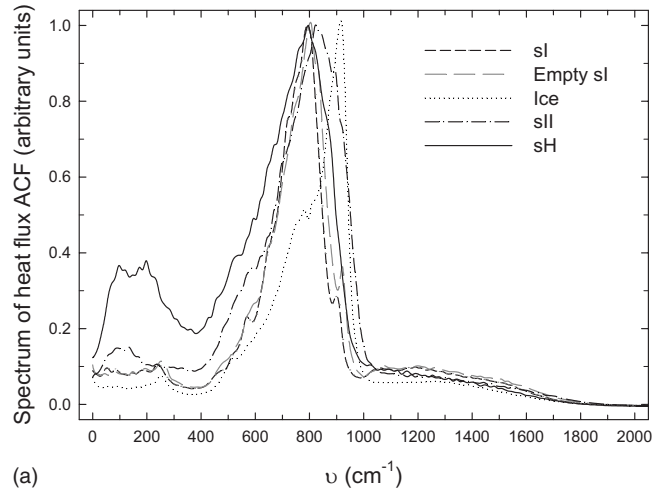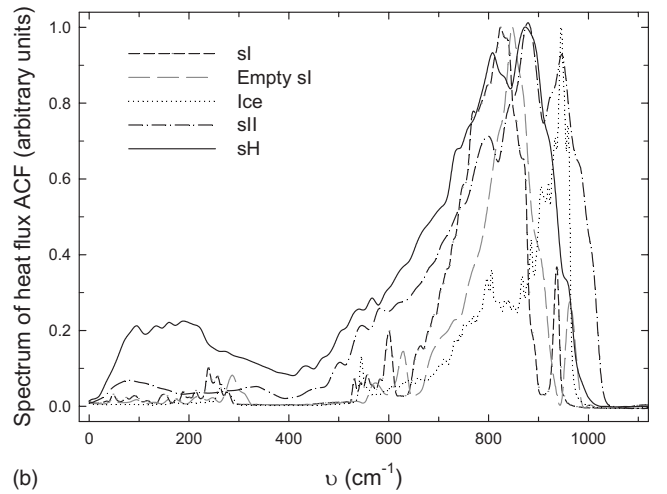

FIG. 3. Long-time normalized JACF's for ice Ih, and sI, sII, sH, and empty sI hydrates at 30 K. Estimates for underlying lattice acoustic-mode's lifetimes are shown, which show good overlap with the corresponding peaks in the oxygen/guest atoms' velocity CF power spectra at 30 K [cf. Figs. 11(b) and 12(b)].

FIG. 4. Power spectra of normalized JACF's at for ice Ih, and sI, sII, sH, and empty sI hydrates at (a) 200 K and (b) 30 K.

rier transformation, using cubic-order end-point corrections applied to the discrete FT for increased accuracy.[45] In Fig. 4, power spectra are specified for each system at 30 and 200 K. The oscillatory features arising from localized optic modes, i.e., water librations, are confirmed by peaks in the 775–950 cm^{-1} range (i.e., the 35–43 fs time-domain oscillations). A spectral peak does not necessary indicate that vibrational mode's involvement in heat transport. In contrast, it reflects its localized nature as an isolated harmonic oscillator. In Fig. 4(a), at high temperature (200 K), the low-frequency region below around 300 cm^{-1} in sI's power spectra is featureless, indicating substantial coupling of water translations with guest vibrations in thermal transport. More distinctive features were observed at lower temperatures [e.g., 30 K, cf. Fig. 4(b)], suggesting the vibrations are more harmonic and dissipate less heat. Strikingly, the optic peak-normalized power spectra for sII, and especially sH, are substantially larger than that of sI in the low-frequency (sub-300 cm^{-1}) region at all temperatures and exhibit vibrational peak frequencies overlapping with lattice and methane vibrational modes, and, importantly, water-methane velocity CCF's as will be shown later. The clear presence of these acoustic vibrational features in the JACF power spectra for sII, and

TABLE III. Optical-modes' angular frequencies (rad/ps), relaxation times (ps), and residual "constant" terms (in $Wm^{-1} K^{-1} fs^{-1}$ for the normalized JACF), based on the fitting procedure. The main mode is specified first, along with its "short" and "long" decay times; in practice, it is this main mode which constitutes almost all of the optical contribution to thermal conductivity. Note: to convert ω (rad/ps) to frequency, ν, in cm^{-1}, multiply by 5.3.

Type	T (K)	ω_1 (rad/ps)	$\tau_{1,1,o}$ (ps)	$\tau_{1,2,o}$ (ps)	c_1	ω_2 (rad/ps)	c_2	ω_3 (rad/ps)	c_3
sI	30	157.6	0.084 ± 0.0092	2.01 ± 0.34	0.0021	176.2	0.0024	112.9	0.0012
	100	154.4	0.061 ± 0.0073	0.82 ± 0.16	0.0016	174.3	0.005	111.2	0.0003
	150	148.3	0.057 ± 0.0061	0.322 ± 0.034	0.0011				
	200	149.8	0.064 ± 0.0074	0.205 ± 0.022	0.0009				
	265	148.3	0.059 ± 0.0085	0.184 ± 0.019	0.0008				
Empty sI	30	160.3	0.085 ± 0.0092	2.3 ± 0.33	0.0045	118.5	0.0012	182.1	0.0028
	100	156.6	0.068 ± 0.0074	0.65 ± 0.082	0.0019	113.7	0.0006	179.5	0.0013
	150	155.1	0.063 ± 0.0061	0.33 ± 0.028	0.0011	112.9	0.0002	176.5	0.0004
	200	151.9	0.059 ± 0.0043	0.305 ± 0.026	0.0008				
	265	148.0	0.053 ± 0.0039	0.16 ± 0.017	0.0003				
Ice	30	178.5	0.13 ± 0.012	2.41 ± 0.31	0.0041	152	0.0022	103.2	0.0007
	100	171.6	0.066 ± 0.005	0.58 ± 0.06	0.0011	153.8	0.0019	104.1	0.0004
	150	174.3	0.060 ± 0.0054	0.234 ± 0.043	0.0009	153.88	0.0025	104.9	0.0002
	200	172.5	0.054 ± 0.0041	0.207 ± 0.023	0.0011				
	220	171.8	0.051 ± 0.0032	0.148 ± 0.011	0.0009				
sII	30	167.8	0.082 ± 0.0084	1.81 ± 0.23	0.011				
	100	166.0	0.073 ± 0.0081	0.58 ± 0.073	0.0062				
	150	159.5	0.062 ± 0.0076	0.238 ± 0.034	0.0048				
	200	155.7	0.044 ± 0.0052	0.173 ± 0.023	0.0028				
	265	155.1	0.059 ± 0.0061	0.184 ± 0.017	0.0015				
sH	30	166.8	0.081 ± 0.0076	1.59 ± 0.21	0.016				
	100	160.3	0.060 ± 0.0058	0.49 ± 0.043	0.0058				
	150	155.7	0.052 ± 0.0048	0.22 ± 0.024	0.0021				
	200	152.3	0.037 ± 0.0034	0.190 ± 0.018	0.0013				
	265	146.6	0.033 ± 0.0029	0.152 ± 0.023	0.0008				

especially SH, indicate less damping of water-methane energy transfer and, consequently, less heat dissipation by the guest molecules. This explains the larger thermal conductivities of sII and sH relative to sI, and their more crystalline temperature dependence (cf. Fig. 1).

C. Analysis of heat-flux ACF's

The heat-flux correlation function can be partitioned into acoustic and optical components. The acoustic part was obtained via reverse transformation of the low-pass filtered FT, omitting the optical region (identified above $350-400$ cm^{-1} in the power spectrum). The optic-modes contribution is obtained by simply removing the acoustic component from the total JACF. The numerical accuracy on the subtraction and subsequent fitting procedures has been taken with great care (see Supplementary Information[48]). The relaxation times, parameters, optic-modes' frequencies, and terms' contributions to the overall predicted thermal conductivity obtained from fittings to the JACF are provided in Tables II and III for ice and each of the hydrate structures, along with experimental conductivity data for ice and sI hydrate.

The acoustic relaxation times in Table III shows that at 30 K all the $\tau_{sh,ac}$ are somewhat similar and increase in the sequence 0.31, 0.32, 0.38, and 0.44–0.47 ps for sH, sII, sI, empty sI hydrates, and ice. At temperatures higher than 100 K, the $\tau_{sh,ac}$ are dramatically different. Both ice and empty sI hydrate show a gradual decrease in $\tau_{sh,ac}$ with increasing temperature, and the relaxation time in empty sI is smaller than in ice. In contrast, the relaxation times in occupied hydrates are significantly shorter and remain nearly constant around 0.05–0.07 ps. The long-range acoustic relaxation time shows a different trend. For ice and empty sI hydrate, two-term acoustic fits (short-range and long-range acoustic, $\tau_{sh,ac}$ and $\tau_{lg,ac}$) are adequate.[46,47] For sI hydrate above 100 K, and for sII and sH above 200 K, a unique additional intermediate-range relaxation time ($\tau_{int,ac}$) achieves a better fit. The long-range, low-frequency $\tau_{lg,ac}$, responsible for the bulk of heat transport, generally decreases with increasing temperature but those of sI and empty sI hydrates are broadly similar and lower than that of ice while sII and sH hydrates have similar relaxation times to ice. In sI, sII, and sH hydrates, $\tau_{int,ac}$'s magnitude (when present) is between $\tau_{sh,ac}$ and $\tau_{lg,ac}$ and is, once again, relatively insensitive to tem-

perature (~0.3–0.4 ps). However, it should be noted that the statistical uncertainties in the $\tau_{int,ac}$'s are comparatively large. In comparison, earlier analysis of tetrahydrofuran hydrate's conductivity with the resonant-scattering model[8] required an additional effective relaxation time of ~0.1 ps to describe heat dissipation via guest rattling. Furthermore, the calculated lifetimes of strongly scattered phonon modes in Xe hydrate[12] are 0.3–1.0 ps. This suggests that the higher-temperature intermediate acoustic relaxation times in sI, sII, and sH hydrates arise from guest-host coupling.

The acoustic and optic relaxation results in Tables II and III also include the contributions arising from analytic integration of the fitted parameters to the normalized JACF, in Eq. (3) (also see Supplementary Material[48]). These are obtained from the zero-frequency values of the analytic real FT (cf. Supplementary Information[48]). The largest contribution to the thermal conductivity is derived from the long-range, low-frequency acoustic term. In sI hydrate above 100 K, and sII and sH hydrates above 200 K, the short and intermediate terms contribute approximate equally. In empty sI hydrate, contributions from the short-range and optic terms are almost equal while the optic contributions are relatively similar for ice, empty sI, sII, and sH hydrates; sI hydrate has a lower optic contribution at all temperatures. For ice Ih at 220 K, the optic contribution is 0.13 Wm^{-1} K^{-1} and accounts for 13% of the total thermal conductivity. The prediction is in excellent agreement with approximately 10% estimated from high-quality experimental data.[50] The amplitude of the residual terms, designated as optical modes, increases at lower temperature (Table III), and more minor optic peaks become apparent in the JACF power spectra [Fig. 4(b) at 30 K].

D. Energy correlation functions

To investigate the underlying magnitude and dynamics of energy-transfer processes, in particular, guest-host transfer, several energy correlation functions were defined. For a purely harmonic system, there is no energy dissipation due to energy transfer between two subsystems. The energy simply exchanged back and forth between the subsystems and the self-energy ACF resembles a harmonic oscillator with no change in the amplitude with time. On the other hand, if energy is dissipated, the amplitude of the ACF will be attenuated (damped) by a decreasing exponential function characterized by the relaxation time of the process. The total "self-energy," averaged over each molecule of each species (water and methane), was computed in each system for each state point at regular intervals. This is defined as the sum of the kinetic energy and all configurational energy interactions involving the species type (obtained readily in the case of long-range electrostatics from Ewald expressions),

$$E_\nu = K_\nu + U_{\nu-\nu} + U_{WM}, \qquad (4)$$

where ν is either water or methane, and it is understood that these quantities are averaged at each point in time over the species' molecules. Normalized autocorrelation functions
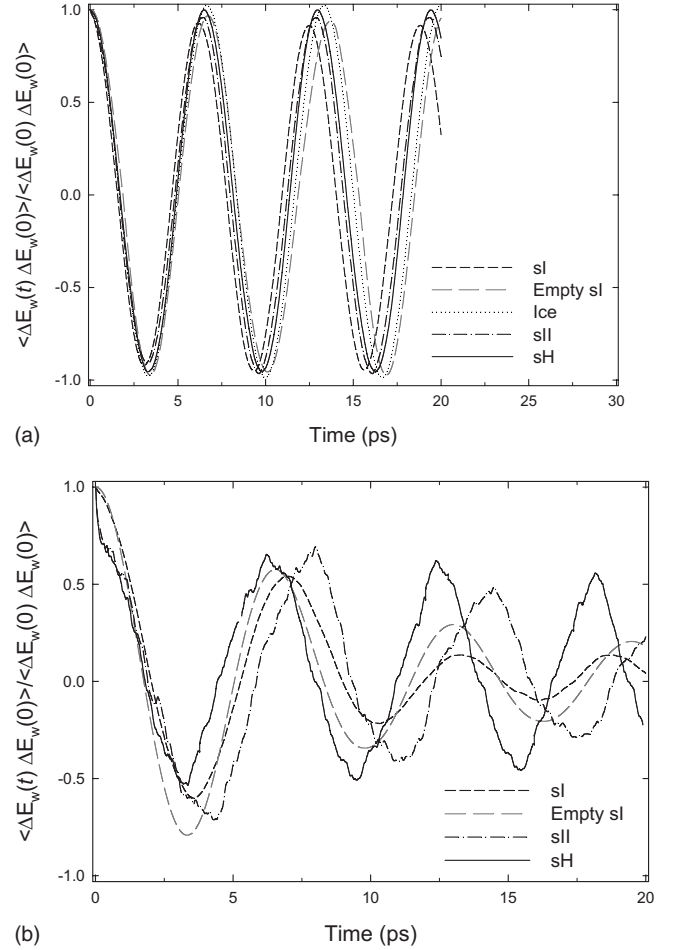

FIG. 5. Normalized ACF of deviations in water self-energies for ice Ih, and sI, sII, sH, and empty sI hydrates at (a) 200 K and (b) 265 K.

were computed in each system for the deviation of the self-energies with respect to their long time, underlying time average, i.e.,

$$\text{ECF}_\nu(t) = \langle\Delta E_\nu(t)\Delta E_\nu(0)\rangle/\langle\Delta E_\nu(0)\Delta E_\nu(0)\rangle, \qquad (5)$$

where

$$\Delta E_\nu(t) = E_\nu(t) - \langle E_\nu(t)\rangle. \qquad (6)$$

Normalized autocorrelation functions were computed in sI, sII, and sH of the deviation of the water-methane interaction energy (composed of electrostatic and van der Waals terms) from its long time, underlying value, i.e.,

$$\text{ECF}_{WM}(t) = \langle\Delta U_{WM}(t)\Delta U_{WM}(0)\rangle/\langle\Delta U_{WM}(0)\Delta U_{WM}(0)\rangle, \qquad (7)$$

where

$$\Delta U_{WM}(t) = U_{WM}(t) - \langle U_{WM}(t)\rangle. \qquad (8)$$

Since the methane-methane energy is very small for singly occupied cages in sI and sII hydrates,[22] this was not considered for those structures. However, the methane-methane interaction energy and the ACF of its deviation was computed for sH, in which there is an occupancy of five methane mol-

TABLE IV. Time-averaged and number-averaged water-methane interaction energies, per methane molecule in sI, sII, and sH. The methane-methane energies are also reported for sH, where the large cage has an occupancy of five. The half amplitude of the essentially periodic variation in the number-averaged interaction energies with respect to their underlying time average are also reported. This is especially periodic at low temperatures. The Lekner method was used to evaluate the electrostatic component of these energies at frequent snapshots over a number of period cycles, to allow subsequent definition of ACF's.

Type	T (K)	$\langle U_{int} \rangle$ (kcal/mol)
sI, wm	30	-5.83 ± 0.266
	100	-5.72 ± 0.197
	150	-5.61 ± 0.145
	200	-5.46 ± 0.091
	265	-5.27 ± 0.071
sII, wm	30	-4.66 ± 0.187
	100	-4.45 ± 0.152
	150	-4.19 ± 0.105
	200	-3.92 ± 0.070
	265	-3.53 ± 0.052
sH, wm	30	-1.60 ± 0.043
	100	-1.40 ± 0.034
	150	-1.17 ± 0.019
	200	-0.94 ± 0.012
	220	-0.57 ± 0.0043
sH, mm	30	-1.91 ± 0.046
	100	-1.70 ± 0.037
	150	-1.45 ± 0.023
	200	-1.21 ± 0.0015
	265	-0.85 ± 0.0060

ecules in the large $5^{12}6^8$ cage. Since the Ewald summation does not evaluate individual pairwise particle-particle interaction energies, a pairwise, highly parallelized implementation of the Lekner summation[24] was used to evaluate the electrostatic component of the water-methane and methane-methane energy deviations at frequent snapshots to allow subsequent definition of their ACF's.

It was found that there was essentially periodic variation in the number-averaged self-energies and interaction energies with respect to their underlying time averages, especially at lower temperatures (Fig. 5). There was an approximately 6.5 ps periodicity in the variation in the energy terms (see below). In Table IV, the average water-methane and s(H) methane-methane interaction energies are reported (per methane molecule), together with the half amplitude of the essentially periodic variation. As expected, sI has the lowest $\langle U_{WM}(t) \rangle$ of -5.27 to -5.83 kcal/mol, owing to the smaller size of its 5^{12} and slightly larger $5^{12}6^2$ cages. $\langle U_{WM} \rangle$ in sII is 67–80 % of $\langle U_{WM} \rangle_{sI}$ while the corresponding proportion for sH is 10–17 % (-0.57 to -1.6 kcal/mol); given the multiple occupancy in the large $5^{12}6^8$ cage, a lower number-averaged interaction energy would be expected. However, $\langle U_{MM} \rangle_{sH}$ is
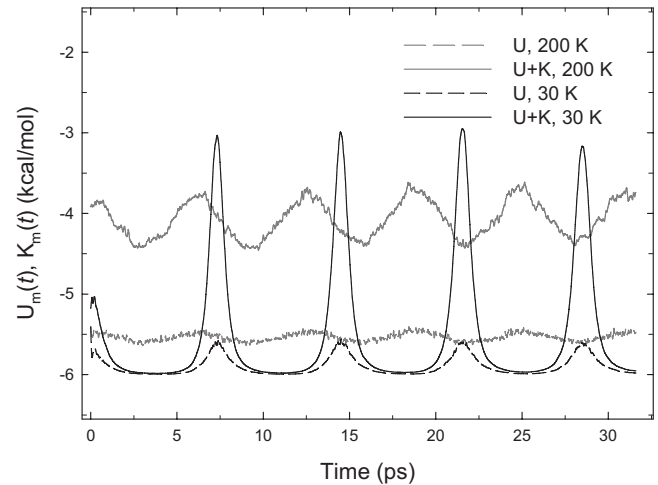

FIG. 6. Variation in underlying potential and kinetic components of methane self-energy, at 30 and 200 K in sI hydrate, averaged at each time over all of the methane molecules. The time average of this methane total self-energy is then subtracted from the total self-energy at each time to allow its ACF to be defined.

some 20–50 % larger than $\langle U_{WM} \rangle_{sH}$, given the contact of five methane molecules per $5^{12}6^8$ cage. Although these interaction energies have not been decomposed to individual cage types, it is still readily apparent that the smaller cages and the resultant more intimate water-methane contact in sI hydrate allow a greater magnitude of guest-host energy transfer.

Plots of the $\text{ECF}_W(t)$ are shown in Fig. 5 for all systems at 200 and 265 K. A 6.5–7 ps periodicity is clearly visible in the ACF's, suggesting that the period of the long-ranged, low-frequency acoustic phonon responsible for the bulk of thermal conduction is of this order. At 200 K, the amplitude of the ACF's remain essentially constant, indicating almost harmonic heat transfer within the water framework. However, the attenuation of amplitude at 265 K, particularly for sI hydrate, indicates some damping and less harmonic transfer within the lattice; it might be expected that the more rapid attenuation for sI is due to its more distorted, weaker hydrogen bonding structure.[61]

To study the time correlation of the methane total self-energies, its underlying time average is subtracted from the total self-energy at each time [cf. Eq. (6) and Fig. 6]. At 30 K, the system behaves in a harmonic way, with the methane molecules reaching maximal and near-zero velocities (the kinetic component) with approximately 7 ps periodicity. The extent of this periodicity is diminished at higher temperature but the low-temperature harmonic energy transfer exhibited by the lattice is also clearly visible in the energetic behavior of the methane molecules.

Normalized ACF's of the deviations in methane self-energies are shown in Fig. 7 for sI, sII, and sH hydrates at (a) 200 K and (b) 265 K. At 200 K, there is essentially harmonic variation in the methanes' self-energy. However, at 265 K, it can be seen that this is no longer the case, and the underlying 6 ps periodicity in energy is no longer as apparent, especially in sII and sH with their larger cages. The time scales for variations in the methane energy correlations at 265 K are in the 0.2–0.6 ps range, which overlap well with the fitted
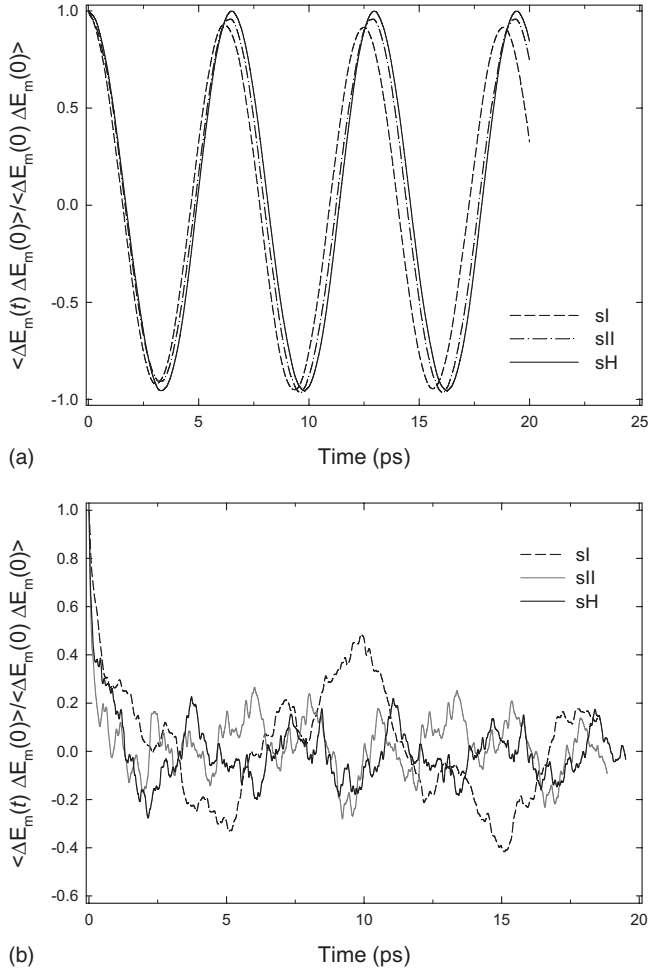
(a)

(b)

FIG. 7. Normalized ACF of deviations in methane self-energies for sI, sII, and sH hydrates at (a) 200 K and (b) 265 K.
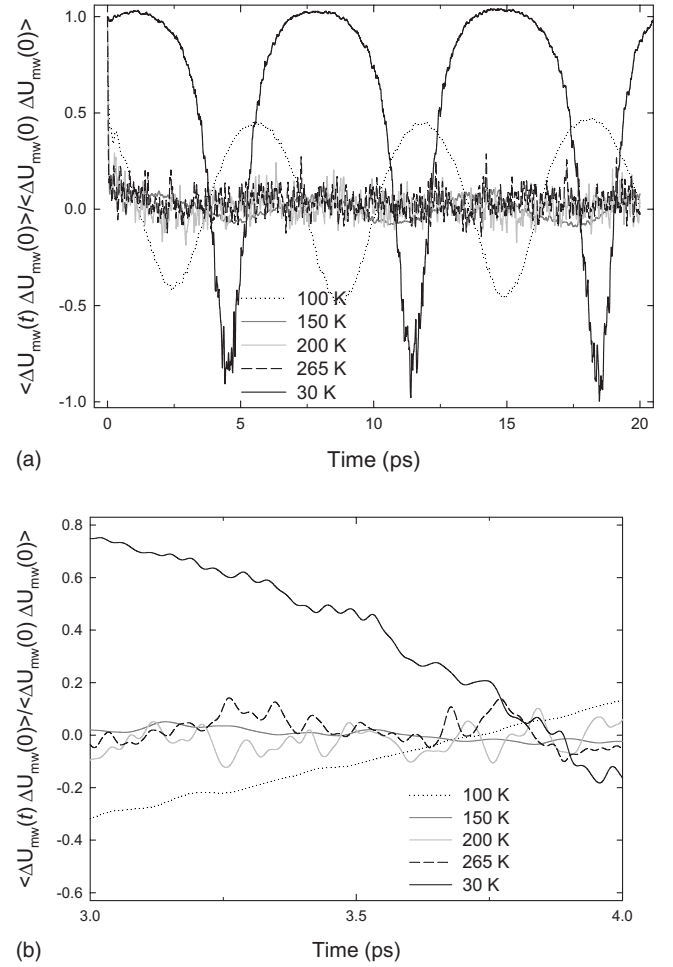

(a)

(b)

FIG. 8. Normalized ACF's of deviations in methane-water interaction energies in sI hydrate between 30 and 265 K (a) over 20 ps and (b) over a shorter time to show sub-picosecond fluctuations more clearly. The Lekner method was used to evaluate the electrostatic component of these energies at frequent intervals over several dozen approximately 6 ps period cycles to define the ACFs.

medium-range acoustic relaxation times of ~ 0.3–0.4 ps, $\tau_{int,ac}$ described above.

The ACF's of the methane-water energy deviation between 30 and 265 K are shown in Fig. 8 for sI hydrate. At 30 and 100 K, the time-correlation functions of this energy deviation are again almost harmonic, indicating no low-temperature heat dissipation. This agrees with the experimental observation that conductivity starts to increase at 90 K,[15] and the predicted results (Fig. 1), together with the introduction of the $\tau_{int,ac}$ in the JACF fits above 100 K. However, above 150 K, strong damping in $ECF_{WM}(t)$ was observed. Moreover, inspection of an enlargement of these ACF's in Fig. 8(b) to examine sub-picosecond fluctuations, a short oscillation period of approximately 0.14 ps was identified, which may be related to the short acoustic relaxation (i.e., $2\tau_{sh,ac}$).[46,47] However, it can be seen readily from Figs. 9 and 10 that the onset of damping in water-methane energy transfer occurs in sII and sH, respectively, above 200 K. This serves to explain why the medium-range acoustic term is only encountered in JACF fits for sII and sH above 200 K (cf. Sec. III C).

In summary, the analysis of the various self-energy and cross-energy correlation functions show that the effect of the guest is only important at high temperature. At low tempera-

ture (e.g., below 100 K), the guest-water energy transfer is largely harmonic and the thermal conductivity is largely governed by the lattice dynamics of the water framework.

E. Velocity correlation functions

Guest-host (methane-water) energy transfer may be investigated from a different perspective via the calculation of velocity autocorrelational (VACF; $m=n$) and cross-(VCCF; $m \neq n$) correlation functions, i.e.,

$$Z(t) = \langle \mathbf{v}_m(0) \cdot \mathbf{v}_n(t) \rangle / \langle \mathbf{v}_m(0) \cdot \mathbf{v}_n(0) \rangle. \quad (9)$$

Velocity correlation functions measure the degree of significance of coupling of atomic motions. If the motions of methane are entirely localized and independent of lattice vibrations, the VCCF between methane and water, $\langle \mathbf{v}_C(t) \cdot \mathbf{v}_O(0) \rangle$, will be damped rapidly (out of phase) and the power spectrum (Fourier transform) of the VCCF shall be featureless. On the other hand, if the motions of the water lattice and the methane are completely correlated, as in an
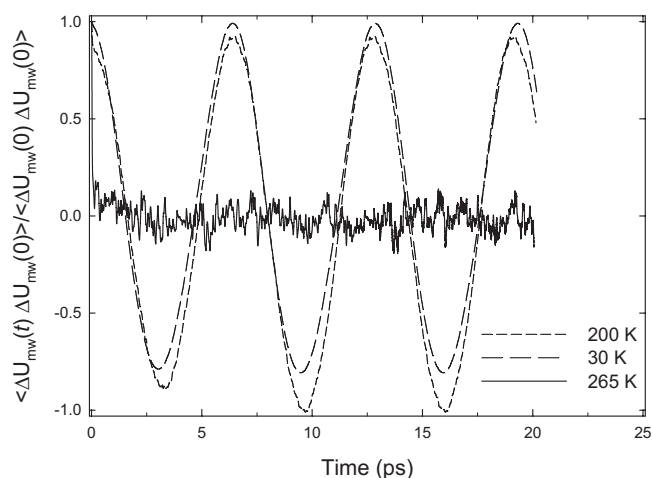
FIG. 9. Normalized ACF's of deviations in methane-water interaction energies in sII hydrate at 30, 200, and 265 K.

extend solid, features in the power pattern of the VCCF will resemble the power spectra obtained from the VACF of the individual components. However, if the power spectrum of the VCCF shows a few distinct sharp features, this indicates that the motions of the methane are only coupled strongly with specific water lattice modes. This provides evidence of resonance scattering.[8]

First, the normalized VACF's of the oxygen and hydrogen atoms in water and of the carbon atoms (i.e., centers of mass) of the methane molecules were evaluated, FT of the VACF's reveal the densities of states; the oxygen atoms in water dominate the translational motion of the lattice while the hydrogen atoms reflect librational motion.[22] The translational vibrations of the encaged methane molecules may be studied in the power spectrum of the methane carbon atoms (centers of mass).

The translational density of states of the lattice is shown in Fig. 11 at 30 and 200 K. The peaks at 60, 175, and 260 cm^{-1} have been assigned to maxima of the transverse-acoustic and longitudinal-acoustic branches and the maxi-
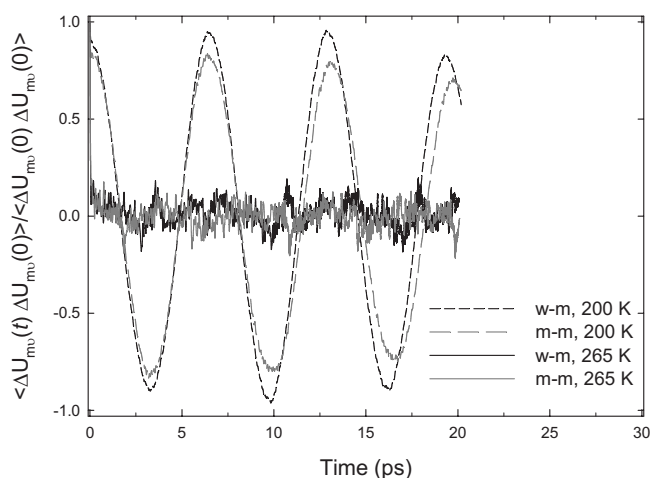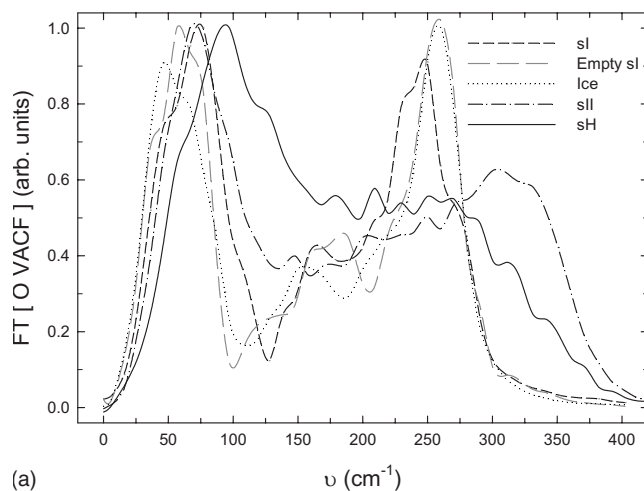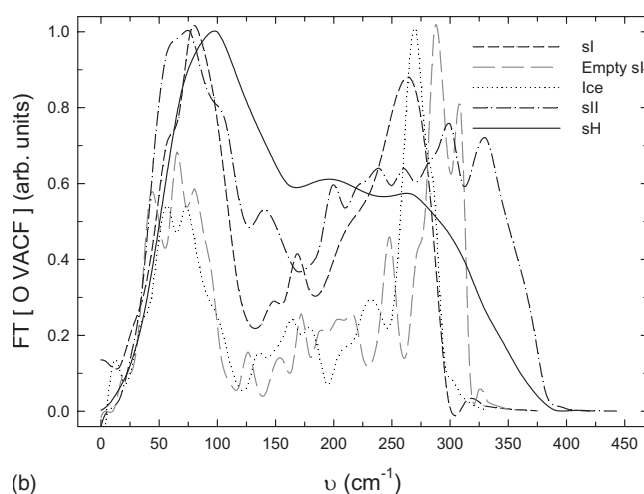

FIG. 10. Normalized ACF's of deviations in methane-water and methane-methane interaction energies in sH hydrate at 200 and 265 K.

FIG. 11. Power spectrum for VACF of oxygen atoms for ice Ih, and sI, sII, sH, and empty sI hydrates at (a) 200 K and (b) 30 K.

mum of the longitudinal-optic branch.[12] It can be seen that the lower acoustic peak frequencies (approximately 50–110 cm^{-1}) overlap approximately with the observed periodicity observed in the residual, long-time JACF (e.g., at 30 K, see Fig. 3, and discussion in Sec. III B). The higher frequency (approximately 250 cm^{-1}) acoustic mode is smaller in magnitude in sII and sH hydrates vis-à-vis the lower-frequency mode but does not appear to correlate to observed periodicity in the JACF's; as will be discussed in Sec. III G, this frequency range does not manifest itself in explicit periodicity in the JACF.

The distinct peaks of the rattling modes in the power spectra of the carbon atoms for sI (Fig. 12) at about 55 and 110 cm^{-1} at 200 K. These frequencies are attributed to methane vibrations in the large and small cages of sI, respectively.[22] However, the guest modes are much less localized and are shifted to higher frequencies in sII and particularly in sH. Broad peaks in the power spectra centered around 150 cm^{-1} in sII were observed. The absence of localized methane rattling vibrations in sH is due to multiple occupancy in the largest cage in sH. There is simply not enough free volume for the methanes to rattle in the cages.
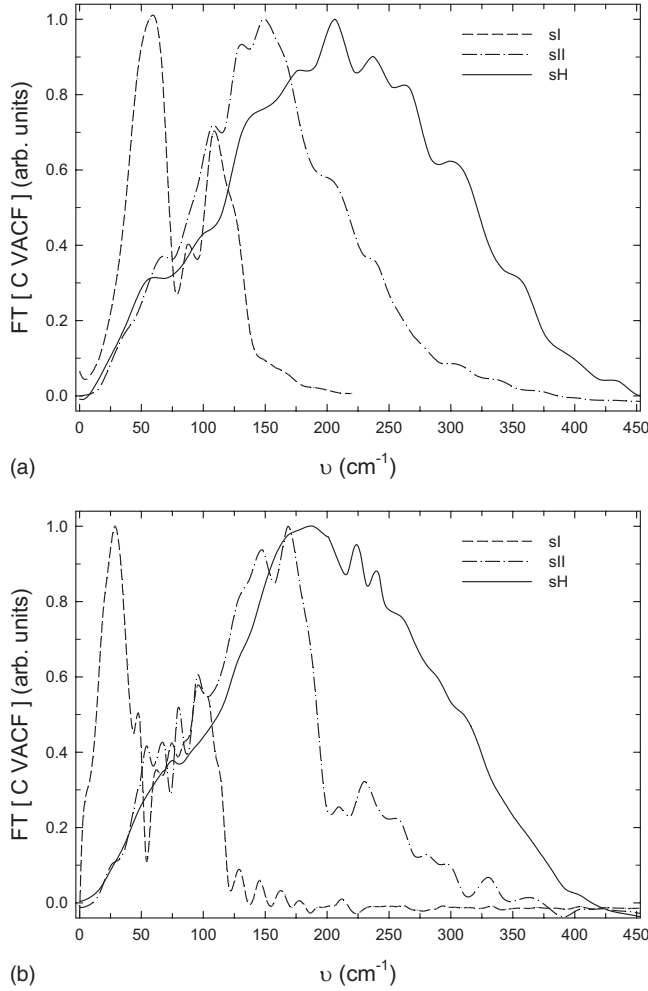
FIG. 12. Power spectrum for VACF of carbon atoms in sI, sII, and sH hydrates at (a) 200 K, (b) 30 K.

FIG. 13. Power spectrum for VCCF between carbon and oxygen atoms in sI, sII, and sH hydrates at (a) 200 K and (b) 30 K.

This observation concurs with the absence of avoided crossing reported in x-ray inelastic-scattering experiments.[57] At 30 K, the methane rattling mode in the sI large cage is reduced to approximately 28 cm^{-1} while the behavior for sII and sH changes relatively little. This indicates that it is the methane rattling modes in the large cages of sI that are subject to the change in resonance-scattering behavior with temperature; there is less scope for substantial changes in small cavities due to the limited space available but the smaller amplitude of displacement at lower temperature in the large cages leads to a lower rattling frequency, as these methane molecules becomes less coupled with the host lattice.

The power spectrum of the O-C VCCF in sI, sII, and sH at 200 and 30 K is shown in Fig. 13. In sI, there are two distinct peaks at 50 and 170 cm^{-1} at 200 K while the corresponding frequencies at 30 K are similar. These vibrations coincide with the maxima of the transverse-acoustic and longitudinal-acoustic frequencies in the O power spectrum, respectively, at these temperatures (cf. Fig. 11).[12] The lack of a spectral feature at 120 cm^{-1}, corresponding to vibrations of methane in the small cages, is highly significant. The absence of a peak infers motions of methane in the small cages are entirely localized and are not coupled to any lattice modes (rattling). The power spectrum of the VCCF of sH
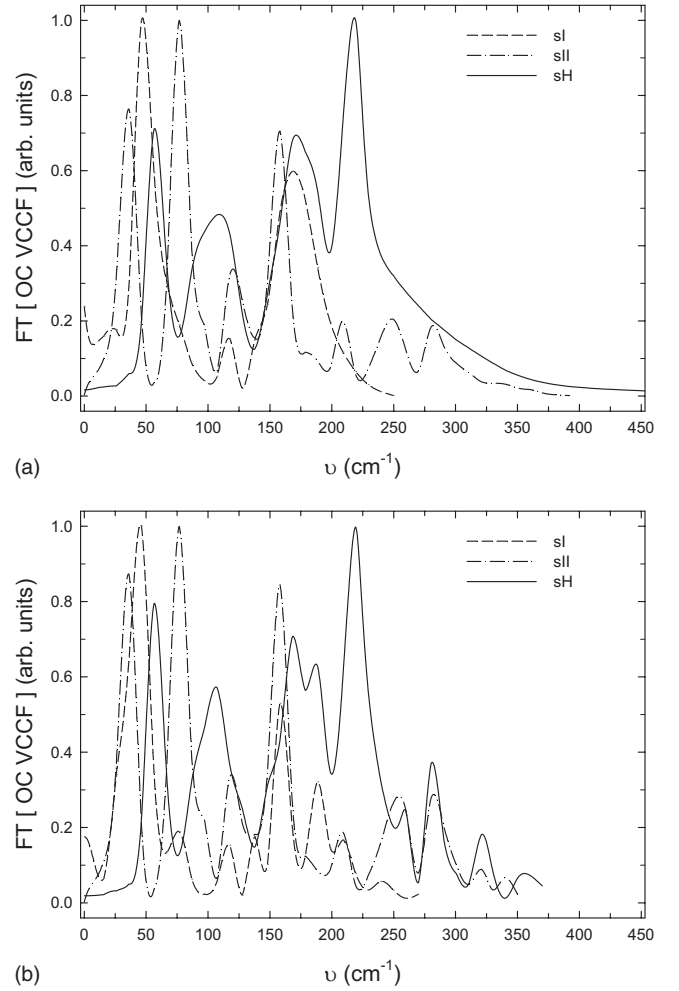
extends over the entire frequency range, indicating that the methane and water vibrations are highly coupled as would be expected for an extended solid. sII shows a somewhat intermediate behavior showing relatively sharp peaks in the FT of the VCCF at 40, 75, and 150 cm^{-1}. The methane is less localized but not to the same extent as sI.

F. Partition of heat-flux vectors

To characterize guest-host interactions further, the JACF was decomposed into contributions due to water and methane. This was accomplished by partitioning the heat-flux vector $\mathbf{J}$ into contributions arising from water and methane molecules, i.e.,

$$\mathbf{J} = \mathbf{J}_W + \mathbf{J}_M. \tag{10}$$

This is described further in the Supplementary Material.[48] Expanding the expression for the JACF (omitting the normalization factor here for convenience), one may assess the equality of integrals of a factorized form

TABLE V. Acoustic relaxation times for the normalized autocorrelation and cross-correlation functions of $\mathbf{J}_w$ and $\mathbf{J}_m$, i.e., with the $V/3k_BT^2$ factor applied to the ACF's and CCF's. These were obtained by using the previous fitting techniques applied to the reverse-filtered CF's, omitting the optic region, which is relatively weak in any case for the $\langle \mathbf{J}_w(t)\cdot \mathbf{J}_m(0)\rangle$ CCF and almost absent for the $\langle \mathbf{J}_m(t)\cdot \mathbf{J}_m(0)\rangle$ ACF.

Type	T (K)	$\langle \mathbf{J}_w(t)\cdot \mathbf{J}_w(0)\rangle$ τ_{sh} (ps)	$\langle \mathbf{J}_w(t)\cdot \mathbf{J}_w(0)\rangle$ τ_{lg} (ps)	$\langle \mathbf{J}_m(t)\cdot \mathbf{J}_m(0)\rangle$ τ (ps)	$\langle \mathbf{J}_w(t)\cdot \mathbf{J}_m(0)\rangle$ τ (ps)
sI	30	0.32 ± 0.054	4.2 ± 0.45	1.28 ± 0.094	0.93 ± 0.12
	100	0.19 ± 0.028	3.4 ± 0.38	0.78 ± 0.085	0.85 ± 0.092
	150	0.072 ± 0.0084	3.3 ± 0.32	0.74 ± 0.069	0.52 ± 0.043
	200	0.054 ± 0.0050	2.8 ± 0.21	0.67 ± 0.071	0.47 ± 0.035
	265	0.051 ± 0.0063	2.3 ± 0.24	0.62 ± 0.065	0.41 ± 0.030
sII	30	0.30 ± 0.022	7.3 ± 0.68	0.145 ± 0.024	0.221 ± 0.035
	100	0.18 ± 0.021	5.0 ± 0.48	0.136 ± 0.022	0.217 ± 0.033
	150	0.076 ± 0.0097	4.0 ± 0.43	0.127 ± 0.019	0.208 ± 0.030
	200	0.061 ± 0.0064	3.7 ± 0.38	0.120 ± 0.021	0.204 ± 0.025
	265	0.051 ± 0.0050	3.2 ± 0.35	0.114 ± 0.015	0.192 ± 0.022
sH	30	0.28 ± 0.048	6.0 ± 0.43	0.047 ± 0.0062	0.187 ± 0.025
	100	0.19 ± 0.031	5.1 ± 0.38	0.044 ± 0.0065	0.183 ± 0.026
	150	0.065 ± 0.0094	3.2 ± 0.30	0.039 ± 0.0060	0.176 ± 0.028
	200	0.052 ± 0.0076	2.9 ± 0.21	0.038 ± 0.0064	0.172 ± 0.023
	265	0.048 ± 0.0062	2.7 ± 0.24	0.038 ± 0.0058	0.156 ± 0.019

$$
\begin{aligned}
\langle \mathbf{J}(t)\cdot \mathbf{J}(0)\rangle &= \langle [\mathbf{J}_W(t)+\mathbf{J}_M(t)]\cdot [\mathbf{J}_W(0)+\mathbf{J}_M(0)]\rangle \\
&\approx \langle \mathbf{J}_W(t)\cdot \mathbf{J}_W(0)\rangle + 2\langle \mathbf{J}_W(t)\cdot \mathbf{J}_M(0)\rangle \\
&+ \langle \mathbf{J}_M(t)\cdot \mathbf{J}_M(0)\rangle .
\end{aligned} \tag{11}
$$

It was found that this equality was essentially true for the hydrate polymorphs, to within $0.02-0.03$ Wm^{-1} K^{-1} (see Supplementary Material[48]).

The acoustic relaxation times for the normalized $\langle \mathbf{J}_w(t)\cdot \mathbf{J}_w(0)\rangle$, $\langle \mathbf{J}_m(t)\cdot \mathbf{J}_m(0)\rangle$, and $\langle \mathbf{J}_w(t)\cdot \mathbf{J}_m(0)\rangle$ are specified in Table V for each case and state point. In general, the methane-water terms contribute more to the thermal conductivity at higher temperatures, with combined percentages increasing steadily from 3% to 8% between 30 and 200 K in the case of sI, and respective values of $2-4$ % and $2-5$ % for sII and sH. Although the water-methane interaction energies are smaller in magnitude for sII and sH (cf. Table IV), the $\langle \mathbf{J}_w(t)\cdot \mathbf{J}_m(0)\rangle$ integral is larger. This is consistent with a smaller damping of this interaction as reflected in the ECF$_{WM}(t)$ in Figs. 8–10. The $\langle \mathbf{J}_m(t)\cdot \mathbf{J}_m(0)\rangle$ integral is also larger than that of $\langle \mathbf{J}_w(t)\cdot \mathbf{J}_m(0)\rangle$ in sH relative to sI and sII, owing to increased interactions of the five methane molecules in the large $5^{12}6^8$ cavity. $\langle \mathbf{J}_w(t)\cdot \mathbf{J}_w(0)\rangle$ has similar relaxation times to the overall JACF, given that water tends to dominate the overall vector (cf. Supplementary Information[48]). Conversely, for sI, the $\langle \mathbf{J}_w(t)\cdot \mathbf{J}_m(0)\rangle$ CCF has a single relaxation time near the full JACF's intermediate range $\tau_{int,ac}$ at 150–265 K ($\sim0.3-0.4$ ps), suggesting medium-range relaxation above 100 K arises from water-methane interactions. In sII and sH, the $\langle \mathbf{J}_w(t)\cdot \mathbf{J}_m(0)\rangle$ relaxation time is somewhat lower at 0.15–0.22 ps, suggesting

faster (as well as less damped) water-methane heat transfer. The lower $\langle \mathbf{J}_m(t)\cdot \mathbf{J}_m(0)\rangle$ relaxation times in sII and sH arise primarily from the presence of larger cages and the multiple occupancy in sH. The increasing importance (from its integral and proportion of overall thermal conductivity) and decreasing relaxation times of $\langle \mathbf{J}_w(t)\cdot \mathbf{J}_m(0)\rangle$ CCF with increasing temperature is, again, an indication of stronger and faster heat dissipation via gust-host interactions.

G. Cumulative-frequency thermal conductivity

To investigate the frequency dependence of the thermal conductivity, the cumulative-frequency thermal conductivity, $K(\omega)$, is obtained by integrating the inverse transformation of the filtered heat flux autocorrelation function (HCACF) spectrum up to ω.[57] Results are shown in Fig. 14 at 30 and 200 K for ice and the hydrate structures, showing three distinct regions separated by arrows. At low frequency, conductivity rises rapidly (I), followed by a relatively "flat" region (II), with steady rises into optical frequencies (III). It should be reminded that frequencies in the Green-Kubo approach are related to phonon-phonon interactions.[46] Region II, approximately $50-300$ cm^{-1}, overlaps with translational vibrations while region III's beginning coincides with the onset of host librations. The ice and empty profiles are quite similar at 30 and 200 K but differ from sI hydrate. In sI hydrate at 200 K, no clear discontinuity was observed between regions II and III, and $K(\omega)$ increases gradually to higher frequencies, emphasizing intermediate relaxation. This was less apparent at 30 K, and for sII and sH hydrates at both temperatures, indicating again the role of the guest and of methane-water interactions in governing thermal behavior.
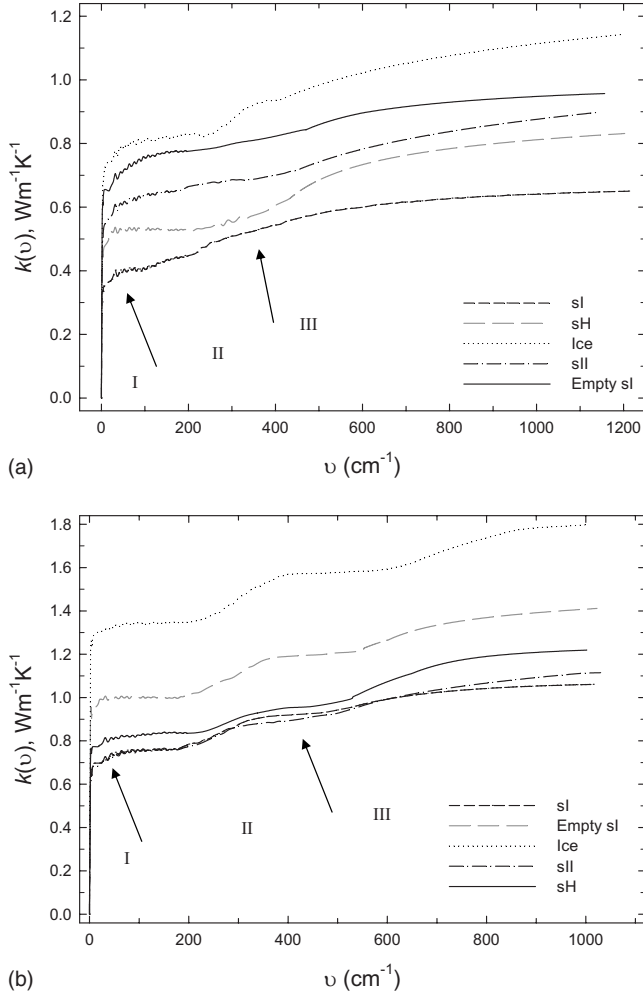
FIG. 14. Cumulative-frequency thermal conductivity $[K(\omega)]$ evaluated from Green-Kubo integral of reverse-transformed low band-pass filtered JACF at each given frequency for ice and sI, sII, sH, and empty sI hydrates at 200 K, at (a) 200 K and (b) 30 K. In both cases, separate frequency regions are indicated for (I) long-range acoustic, (II) medium-range to short-range acoustic, and (III) optic behavior.

The approximately 6 ps (i.e., about 5 cm^{-1}) periodicity evident in the energy ACF's appears to be correlated with that of the long-range, low-frequency acoustic mode which is responsible for the bulk of the thermal conductivity. This was established by finding a very low (less than 0.05 Wm^{-1} K^{-1}) thermal conductivity for reverse-transformed JACF's whose spectrum had been retained substantially below 5 cm^{-1} (i.e., 1–2 cm^{-1}), with a sudden rise to within 70% of the previously fitted analytic long-range contribution for filtering out the power spectrum above 3–6 cm^{-1}; this is shown in Fig. 14 and Table II. The increase in short-range acoustic contribution to the (reverse-filtered) JACF was found to halt once the cutoff frequency in the power spectrum increased beyond about 250 cm^{-1} upon reverse transformation. There were no periodic oscillations in the reverse-filtered JACF until beyond 350–400 cm^{-1}, corresponding to the onset of the optical region; this underlines further the approximate relationship between Green-Kubo frequencies and the phonon frequencies.

Inspection of Fig. 14 and Table III reveals that sI hydrate has a lower optical contribution (approximately 50%) vis-à-vis ice and other polymorphs. However, the empty sI structure has an optical component similar in magnitude to ice and sII and sH hydrates. This may be rationalized in terms of the effects that presence of the methane molecules has on the librational density of states of the lattice. Inspection of the power spectra of the hydrogen atoms in empty and occupied sI hydrates at 200 K (cf. Fig. S5, Supplementary Information[48]) shows the presence of methane weakens the water lattice and shifts the maximum energy cutoff of the librational vibrations by 80 cm^{-1} (1000 cm^{-1} vs 920 cm^{-1}) to lower frequencies. The weakened lattice librations' modes reduce the efficiency of optical phonons' propagation through the lattice, thereby lowering the optical component of thermal conductivity.

IV. CONCLUSIONS

The experimental thermal conductivities of ice, empty sI hydrate, and sI, sII, and sH hydrates have been reproduced semiquantitatively by the rigorous GK approach with accurate long-range electrostatics. Significantly, the observed reversal in sI's temperature dependence at 90 K is predicted. Through comprehensive analysis of heat-flux correlation functions, the guests' role in heat-transport dissipation in sI hydrate above 100 K, and to a lesser extent in sII and sH above 200 K, is demonstrated clearly. Since the (van der Waals) water-methane interaction is weak (cf. Table IV), scattering of thermal phonons is much more efficient at higher temperature ($>$100 K) in sI. However, the less intimate water-methane contact in the larger cavities in sII and sH hydrates means that the temperature required for significant dissipation in water-methane energy transfer is above 200 K, as larger-amplitude thermal rattling of the methane molecules at higher temperature is needed to bring about the intermittent close guest-host contact required for dissipation in larger cavities with more free space. Calculations also show empty sI's conductivity behavior is similar to ice, except with lower absolute values: this is due mainly to smaller long-range relaxation times $\tau_{lg,ac}$ (Table II), indicating shorter phonon mean-free paths. A similar observation has been made in zeolites, with distortions of SiO_4 suggested as the cause.[47] In hydrates, the water framework is much more distorted[61] and therefore the hydrogen-bond network is more strained than in ice; this would result in inhibition of long-range modes and spatial localization of energy. If correct, this conjecture suggests that low thermal conductivity depends not only on guest-host interactions but is also related to rigidity of the framework. This helps to rationalize the apparent absence of resonant scattering in some semiconductor clathrates and skutterudites and low conductivity in empty silicon clathrate; in particular, skutterudites constitute potential candidates of a new class of engineered efficient thermoelectric materials guided by the principle of phonon glass electron crystals.[9,10]

ACKNOWLEDGMENTS

---

*Corresponding author.

†niall.english@ucd.ie

‡john.tse@usask.ca

§Present address: Chevron Ltd., Pembroke SA71 5SJ, Great Britain.

[1] Y. F. Makogon, *Hydrates of Hydrocarbons* (PennWell Books, Tulsa, Oklahoma, 1997).

[2] E. D. Sloan and C. A. Koh, *Clathrate Hydrates of Natural Gases*, 3rd revised ed. (CRC, USA/Taylor & Francis, USA, 2007).

[3] S. Alavi, J. A. Ripmeester, and D. D. Klug, J. Chem. Phys. **126**, 124708 (2007).

[4] G. J. MacDonald, Annu. Rev. Energy Environ. **15**, 53 (1990).

[5] K. A. Kvenvolden, Chem. Geol. **71**, 41 (1988).

[6] I. M. Chou, A. Sharma, R. C. Burruss, J. Shu, H.-K. Mao, R. J. Hemley, A. F. Goncharov, L. A. Stern, and S. H. Kirby, Proc. Natl. Acad. Sci. U.S.A. **97**, 13484 (2000).

[7] R. G. Ross, P. Andersson, and G. Bäckström, Nature (London) **290**, 322 (1981).

[8] J. S. Tse and M. A. White, J. Phys. Chem. **92**, 5006 (1988).

[9] G. A. Slack, in *Thermoelectric Materials—New Directions and Approaches*, MRS Symposia Proceedings Vol. 478, edited by T. M. Tritt, M. G. Kanatzidis, H. B. Lyon, and G. D. Mahan, (Materials Research Society, Pittsburgh, 1997), pp. 47–54.

[10] G. S. Nolas, D. T. Morelli, and T. M. Tritt, Annu. Rev. Mater. Sci. **29**, 89 (1999).

[11] J. S. Tse, C. I. Ratcliffe, B. M. Powell, V. P. Sears, and Y. P. Handa, J. Phys. Chem. A **101**, 4491 (1997).

[12] J. S. Tse, V. P. Shpakov, V. R. Belosludov, F. Trouw, and Y. P. Handa, Europhys. Lett. **54**, 354 (2001).

[13] J. Baumert, C. Gutt, V. P. Shpakov, J. S. Tse, M. Krisch, M. Müller, H. Requardt, D. D. Klug, S. Janssen, and W. Press, Phys. Rev. B **68**, 174301 (2003).

[14] J. S. Tse, D. D. Klug, J. Y. Zhao, W. Sturhahn, E. E. Alp, J. Baumert, C. Gutt, M. R. Johnson, and W. Press, Nature Mater. **4**, 917 (2005).

[15] A. I. Krivchikov, B. Ya. Gorodilov, O. A. Korolyuk, V. G. Manzhelii, H. Conrad, and W. Press, J. Low Temp. Phys. **139**, 693 (2005).

[16] J. L. Cohn, G. S. Nolas, V. Fessatidis, T. H. Metcalf, and G. A. Slack, Phys. Rev. Lett. **82**, 779 (1999).

[17] D. C. Rapaport, *The Art of Molecular Dynamics Simulation*, 2nd ed. (Cambridge University Press, Cambridge, 2004).

[18] W. L. Jorgensen, J. Chandrasekhar, J. D. Madura, R. W. Impey, and M. L. Klein, J. Chem. Phys. **79**, 926 (1983).

[19] W. L. Jorgensen, D. S. Maxwell, and J. Tirado-Rives, J. Am. Chem. Soc. **118**, 11225 (1996).

[20] R. Sun and Z. H. Duan, Geochim. Cosmochim. Acta **69**, 4411 (2005).

[21] E. A. Mastny and J. J. de Pablo, J. Chem. Phys. **129**, 034701 (2008).

[22] N. J. English and J. M. D. MacElroy, J. Comput. Chem. **24**, 1569 (2003).

[23] H. Jiang, K. D. Jordan, and C. E. Taylor, J. Phys. Chem. B **111**, 6486 (2007).

[24] N. J. English, Mol. Phys. **106**, 1887 (2008).

[25] S. W. de Leeuw, J. W. Perram, and E. R. Smith, Proc. R. Soc. London, Ser. A Math. Phys. Sci. **373**, 27 (1980).

[26] M. P. Allen and D. J. Tildesley, *Computer Simulation of Liquids* (Clarendon, Oxford, 1987).

[27] H. C. Andersen, J. Comput. Phys. **52**, 24 (1983).

[28] W. G. Hoover, Phys. Rev. A **31**, 1695 (1985).

[29] S. Melchionna, G. Ciccotti, and B. L. Holian, Mol. Phys. **78**, 533 (1993).

[30] R. K. McMullan and G. A. Jeffrey, J. Chem. Phys. **42**, 2725 (1965).

[31] T. C. W. Mak and R. K. McMullan, J. Chem. Phys. **42**, 2732 (1965).

[32] K. A. Udachin, C. I. Ratcliffe, G. D. Enright, and J. A. Ripmeester, Supramol. Chem. **8**, 173 (1997).

[33] J. A. Hayward and J. R. Reimers, J. Chem. Phys. **106**, 1518 (1997).

[34] J. D. Bernal and R. H. Fowler, J. Chem. Phys. **1**, 515 (1933).

[35] A. Rahman and F. H. Stillinger, J. Chem. Phys. **57**, 4009 (1972).

[36] Y. Okano and K. Yasuoka, J. Chem. Phys. **124**, 024510 (2006).

[37] E. J. Rosenbaum, N. J. English, J. K. Johnson, D. W. Shaw, and R. P. Warzinski, J. Phys. Chem. B **111**, 13194 (2007).

[38] J. A. Izaguirre, S. Reich, and R. D. Skeel, J. Chem. Phys. **110**, 9853 (1999).

[39] C. Vega, E. Sanz, and J. L. F. Abascal, J. Chem. Phys. **122**, 114507 (2005); J. L. F. Abascal and C. Vega, *ibid.* **123**, 234505 (2005); R. G. Fernández, J. L. F. Abascal, and C. Vega, *ibid.* **124**, 144506 (2006).

[40] P. J. Daivis and D. J. Evans, Mol. Phys. **81**, 1289 (1994).

[41] R. Vogelsang and C. Hoheisal, Phys. Rev. A **35**, 3487 (1987).

[42] J. Petravic, J. Chem. Phys. **123**, 174503 (2005).

[43] N. Galamba, C. A. Nieto de Castro, and J. F. Ely, J. Phys. Chem. B **108**, 3658 (2004).

[44] D. J. Evans and G. P. Morriss, *Statistical Mechanics of Nonequilibrium Liquids* (Academic, San Diego, 1990).

[45] W. H. Press, B. P. Flannery, S. A. Teukolsky, and W. T. Vetterling, *Numerical Recipes*, 2nd ed. (Cambridge University Press, Cambridge, 1992).

[46] A. J. H. McGaughey and M. Kaviany, Int. J. Heat Mass Transfer **47**, 1783 (2004).

[47] A. J. H. McGaughey and M. Kaviany, Int. J. Heat Mass Transfer **47**, 1799 (2004).

[48] See EPAPS Document No. E-PRBMDO-80-010937 for a detailed description of the heat-flux ACF fitting procedure, partitioning of the heat flux vector, and additional power spectra. For more information on EPAPS, see http://www.aip.org/pubservs/epaps.html.

[49] W. F. Waite, L. A. Stern, S. H. Kirby, W. J. Winters, and D. H. Mason, Geophys. J. Int. **169**, 767 (2007).

[50] G. A. Slack, Phys. Rev. B **22**, 3065 (1980).

[51] T. M. Tritt, *Thermal Conductivity: Theory, Properties, and Applications* (Kluwer Academic, /Plenum, New York, 2004).

[52] A. J. H. McGaughey and M. Kaviany, Adv. Heat Transfer **39**, 169 (2006).

[53] J. S. Tse, J. Phys. Colloq. **48**, 543 (1987).

[54] R. Inoue, H. Tanaka, and K. Nakanishi, J. Chem. Phys. **104**, 9569 (1996).

[55] L. Hernández de la Pena, M. S. Gulam Razul, and P. G. Kusalik, J. Chem. Phys. **123**, 144506 (2005).

[56] O. Andersson, Phys. Rev. B **65**, 140201(R) (2002; Phys. Chem. Chem. Phys. **7**, 1441 (2005).

[57] J. Baumert, C. Gutt, M. Krisch, H. Requardt, M. Müller, J. S. Tse, D. D. Klug, and W. Press, Phys. Rev. B **72**, 054302 (2005).

[58] A. I. Krivchikov, B. Ya. Gorodilov, A. Korolyuk, V. G. Manzhelii, O. O. Romantsova, H. Conrad, W. Press, J. S. Tse, and D. D. Klug, Phys. Rev. B **73**, 064203 (2006).

[59] H. Jiang, E. Myshakin, K. D. Jordan, and R. P. Warzinski, J. Phys. Chem. B **112**, 10207 (2008).

[60] A. J. C. Ladd, W. Moran, and W. G. Hoover, Phys. Rev. B **34**, 5058 (1986).

[61] C. Gutt, B. Asmussen, W. Press, M. R. Johnson, Y. P. Handa, and J. S. Tse, J. Chem. Phys. **113**, 4713 (2000).